

# 1      Turbulent mixing and dissipation around rough 2      seamounts

3      **Tomas Chor<sup>1,2</sup>, Jacob Wenegrat<sup>1</sup>, and Gregory L. Wagner<sup>3,4</sup>**

4      <sup>1</sup>Department of Atmospheric and Oceanic Science, University of Maryland, College Park, MD, USA

5      <sup>2</sup>atdepth MRV Inc., Cambridge, MA, USA

6      <sup>3</sup>Massachusetts Institute of Technology, Cambridge, MA, USA

7      <sup>4</sup>Aeolus Labs, San Francisco, CA, USA

## 8      **Key Points:**

- 9      • Small-scale topographic roughness can increase dissipation in seamount wakes by  
10     up to tenfold and enhance mixing by a factor of three
- 11     • This effect is most pronounced for seamounts typical of the Southern Ocean
- 12     • Globally, this difference accounts for 30% of kinetic energy dissipation by seamounts

**Abstract**

Seamounts are critical components of the global ocean energy budget, contributing significantly to turbulent dissipation through their interaction with large-scale flows. However, most previous numerical investigations used smoothed bathymetry that omit small scale topographic variability. Here we use turbulence-resolving large-eddy simulations to investigate how bathymetric roughness affects seamount wake energetics. We compare flows around realistic, rough seamounts against versions smoothed over varying horizontal scales and find that dissipation and mixing rates can differ by up to an order of magnitude between cases. Importantly, seamounts in the parameter regimes where roughness effects are most pronounced (low Slope Burger numbers) are concentrated in the Southern Ocean, coinciding with very fast flows and resulting in leading order effects for global dissipation due to seamounts. An implication of our results is that model horizontal spacings of at least order 100 meters may be necessary to capture the full energetics in most seamount wakes in the Southern Ocean.

**Plain Language Summary**

Seamounts are underwater mountains that play an important role in mixing ocean waters, which affects how the ocean circulates and how heat and nutrients move around the globe. Until now, computer models have usually used smooth versions of seamounts, ignoring their rough, bumpy surfaces. In this study, we use advanced high-resolution simulations to show that including small-scale roughness on seamounts can greatly increase the amount of mixing and energy loss in the ocean—sometimes by as much as a factor of ten. This effect is especially strong for seamounts located in the Southern Ocean, where currents are particularly fast. Our results suggest that many current estimates may be missing a significant portion of the mixing and dissipation caused by seamounts, and that small details on the seafloor can have big impacts on the ocean’s energy budget.

**1 Introduction**

Seamounts, underwater mountains rising from the seafloor, have emerged as critical components of the global ocean mixing system with far-reaching implications for ocean circulation and biogeochemical budgets (Munk & Wunsch, 1998; Mashayek et al., 2024). Due to their interactions with the bottom flow, they stir and mix deep waters by many processes, including lee waves (Nikurashin et al., 2014; Wright et al., 2014; Perfect et al., 2020b) and topographic wake vortices (Perfect et al., 2018; Srinivasan et al., 2019; Perfect et al., 2020a; Nagai et al., 2021). The ensuing dissipation and mixing are thought to exert important control on the rate and structure of the overturning circulation, likely playing an important role in the upwelling of deep waters and global energetics (Waterhouse et al., 2014; Mashayek et al., 2024).

Previous investigations using regional models have revealed the complex dynamics and mixing patterns around seamounts (Perfect et al., 2018; Srinivasan et al., 2019; Perfect et al., 2020a; Srinivasan et al., 2021). Collectively, they show that rotation and stratification play an important role in shaping the dynamics and energetics of flows around them. For example, above a critical Burger number, vortex shedding frequency varies vertically with local seamount diameter, resulting in vertically-decoupled vortices and a vertically-sheared wake (Perfect et al., 2018). This in turn drives different energetic transfers from unsheared quasigeostrophic motions (Perfect et al., 2020a). Different combinations of rotation and stratification also lead to different dynamical instabilities, which can also shape flow energetics (Srinivasan et al., 2019, 2021). Submesoscale centrifugal instabilities are often present as a particularly energetic example (Srinivasan et al., 2019), in dynamics that were also seen in observations (Nagai et al., 2021) and near coastal bathymetric shapes (Gula et al., 2016; Chor & Wenegrat, 2025). Similar conclusions were reached by Liu et al. (2024) using turbulence-resolving simulations of a conical seamount, with

63 the caveat that the authors saw vertical coupling, even past the critical Burger number  
 64 found by Perfect et al. (2018) — an indication that geometry may play an important role.  
 65 Finally, Puthan et al. (2022) used similar turbulent simulations to investigate the effect  
 66 of tides, finding complex dynamics that depend strongly on both tidal phase and strength.

67 Common to all the aforementioned studies is the assumption of idealized, smooth  
 68 seamount geometries, which has been the standard approach in both theoretical and nu-  
 69 matical investigations of seamount-flow interactions. Even in investigations using real-  
 70 istic bathymetry (Mashayek et al., 2024), seamounts are implicitly smoothed by the in-  
 71 herent resolution of regional models and often further (explicitly) smoothed to avoid er-  
 72 rors in sigma-coordinate models (Mellor et al., 1998; Sikirić et al., 2009). However, in-  
 73 vestigations from the atmospheric science community suggest that small-scale features  
 74 on mountains play a crucial role in modulating energy dissipation and flow dynamics,  
 75 with implications that should parallel those found in oceanic systems. In atmospheric  
 76 flows over complex terrain, unresolved subgrid-scale topography generates significant drag  
 77 forces and dissipation that often needs to be parameterized in global circulation mod-  
 78 els (Lott & Miller, 1997; Scinocca & McFarlane, 2000). Furthermore, small-scale details  
 79 of mountains have been shown to change dynamics in both numerical and observational  
 80 experiments (Aebischer & Schär, 1998; Schär, 2002; Schär et al., 2003), suggesting sim-  
 81 ilar effects may likewise occur for seamounts. Indeed, recent work has indicated that pa-  
 82 rameterized turbulent mixing is increased in hydrostatic simulations of a seamount that  
 83 partially resolve the fine scale topographic variability (Aghor et al., 2025). Since our abil-  
 84 ity to represent these high dissipation rates is fundamentally limited by resolution con-  
 85 straints, especially in global and regional ocean models, the impacts of seamount (and,  
 86 more generally, topography) roughness should be well-understood, so that they can be  
 87 taken into account when appropriate.

88 In this paper we use Large-Eddy Simulations (LES) to show that resolved rough-  
 89 ness can significantly modify seamount wake energetics, often leading to differences larger  
 90 than an order of magnitude. We focus our detailed analysis on the case of weakly strat-  
 91 ified, rotating seamounts in Section 3 (since they are the most affected by small-scale rough-  
 92 ness), where we show that small-scale bathymetric variation can increase kinetic energy  
 93 (KE) dissipation by an order of magnitude, while increasing mixing by a factor of three.  
 94 We also run a general parameter sweep in Section 4, and use results to investigate im-  
 95 plications for global energetics in Section 5. Specifically, because the seamounts whose  
 96 energetics are impacted by roughness are concentrated in the energetic flows of the South-  
 97 ern Ocean, we estimate that up to 30% of the total dissipation by seamounts globally  
 98 may be attributed to small-scale bathymetric variability.

## 99 2 Computational model and simulations

100 We use turbulence-resolving Large-Eddy Simulations (LES) implemented using the  
 101 Julia package Oceananigans (Ramadhan et al., 2020; Wagner et al., 2025) for all sim-  
 102 ulations in this work. The simulations solve the filtered nonhydrostatic incompressible  
 103 Boussinesq equations with subgrid-scale turbulence modeled using a Lagrangian-averaged  
 104 dynamic Smagorinsky closure (Bou-Zeid et al., 2005). The domain is periodic in the merid-  
 105 ional direction with inflow-outflow conditions in the zonal direction and an immersed bound-  
 106 ary method to represent the bathymetry. Complete details on the numerical implemen-  
 107 tation, boundary conditions, and discretization — including specific schemes, pressure  
 108 treatment, SGS closure, and grid structure — are provided in Section 1 of the Sup-  
 109 porting Information (Adcroft et al., 1997; Chamecki et al., 2019; Bou-Zeid et al., 2005; Kleissl  
 110 et al., 2006; Ramadhan et al., 2020; Wagner et al., 2025) and some key quantities can  
 111 be found in Table 1.

112 At the origin of our coordinate system there is a seamount whose bathymetric data  
 113 was taken from the *Balanus* seamount (of the New England seamounts) using the Global

Parameter	Definition	Value
$L_x$	Domain length (zonal)	3500 m
$L_y$	Domain length (meridional)	2000 m
$L_z$	Domain height (vertical)	200 m
$\Delta x, \Delta y$	Horizontal grid spacing	2 m
$\Delta z$	Vertical grid spacing for $z \in [0, H]$	1 m
$U_\infty$	Background velocity	$0.1 \text{ m s}^{-1}$
$N_\infty$	Background stratification	(varies)
$f$	Coriolis frequency	(varies)
$L$	Smoothing scale	(varies)
$W$ (FWHM)	Seamount width (Full Width at Half Maximum)	500 m
$H$	Seamount height	100 m
$Ro_b$	Bathymetric Rossby number ( $U_\infty /  f W$ )	(varies)
$Fr_b$	Bathymetric Froude number ( $U_\infty / N_\infty H$ )	(varies)
$S_b$	Slope Burger number ( $Ro_b / Fr_b = N_\infty H /  f W$ )	(varies)

Table 1: Parameters used by simulations in the present work along with their definitions and values. The smoothing scale  $L$  refers to the resolution at which bathymetry is coarsened before interpolation back to the high-resolution grid (in order to smooth it). Note that Mashayek et al. (2024) define their Burger number as the square of  $S_b$ .

114 Multi-Resolution Topography Synthesis (Ryan et al., 2009). Balanus was chosen because  
 115 it is very well-surveyed and has an approximately Gaussian shape, facilitating comparisons  
 116 with other idealized studies. Note that, in order to generalize the horizontal scale  
 117 to non-idealized seamounts, we use the Full Width at Half Maximum (FWHM<sup>1</sup>) as the  
 118 relevant horizontal width  $W$  (calculated here as the square root of the seamount area  
 119 at half its height).

120 Given the constraints of LES (which needs to have  $\mathcal{O}(1)$  meter resolution in the  
 121 ocean), the seamount was scaled down to fit into a computationally-feasible domain size.  
 122 This approach is standard in the literature and is equivalent to running a dimensionless  
 123 simulation (Puthan et al., 2022; Liu et al., 2024), which conserves dynamics in high enough  
 124 Reynolds number flows (Jalali & Sarkar, 2017; Chor & Wenegrat, 2025). One require-  
 125 ment for dynamical similarity in our case is that the (attached) bottom boundary layer  
 126 thickness needs to be much smaller than the size of the obstacle, which is observed. To  
 127 make implications more intuitive, we occasionally scale up our results to match typical  
 128 seamount dimensions when presenting key results — typically FWHM =  $W = 10$  km  
 129 (S. Kim & Wessel, 2011). We indicate when this occurs; otherwise, results use the sim-  
 130 ulation dimensions.

131 Note also that we can rescale the seamount independently in the vertical and hor-  
 132 izontal directions, giving us control of the aspect ratio  $\delta = H/W$ . This allowed us to  
 133 try simulations using Balanus with different aspect ratios, where we verified that  $\delta$  has  
 134 only a small impact on wake energetics of simulations for ocean-relevant values. Instead  
 135 the main dynamical consequence of a higher  $\delta$ , is that it limits the permitted range of  
 136 lee waves, which are only allowed when  $|f| < U_\infty k < N_\infty = S_b |f| / \delta$ , where  $k$  is a  
 137 horizontal perturbation wavenumber, dictated in our case by the seamount (Baker & Mashayek,  
 138 2022). Thus, no lee waves are allowed when  $\delta \geq S_b$ . Given that preliminary investiga-  
 139 tions indicate that the presence of waves does not significantly modify our major find-  
 140 ings (see Section 2 of the Supporting Information), we use  $\delta = 0.2$  in our simulations,

<sup>1</sup> For a symmetric Gaussian seamount, FWHM =  $2\sqrt{\ln 2}D$ , where  $D$  is the Gaussian diameter.

141 excluding lee waves. Finally, simulations were run where the flow impinges on the seamount  
 142 at different angles, with no appreciable differences observed in the results, suggesting that  
 143 the effects discussed here are likely independent of specific bathymetric features.

144 The bottom geometry is depicted in the top row of Figure 1, with the original seamount  
 145 shown in the left panel and a smoothed version (with a smoothing scale  $L = 0.8W$ ) shown  
 146 in the right panel. The smoothing, whose purpose is discussed in Sections 3 and 4, was  
 147 performed by coarsening the original bathymetry data to a given resolution (named the  
 148 smoothing scale  $L$ ) and interpolating it back into the original high-resolution grid, which  
 149 mimics the smoothed geometries used in idealized studies, and missing subgrid-scale vari-  
 150 ance inherent in larger-scale realistic modeling.

### 151 3 Low- $S_b$ seamounts (representative of the Southern Ocean)

152 We start our analysis focusing on seamounts that have a moderately low Slope Burger  
 153 number  $S_b$ . As will be shown in Section 4, the energetics of seamounts in this regime are  
 154 highly sensitive to roughness. Furthermore, taking data from Mashayek et al. (2024) as  
 155 a basis, we see these seamounts are common in the Southern Ocean, which experiences  
 156 especially energetic flows. Given that the total contribution to dissipation by an indi-  
 157 vidual seamount can be estimated as

$$\iiint \varepsilon_k dx dy dz \propto U_\infty^3 W^2, \quad (1)$$

158 we expect such a regime to be particularly important for global energetics given the cu-  
 159 bic dependence on velocity (see also Section 5 for a quantitative assessment).

160 We simulate a seamount interaction with  $Ro_b = 0.1$ ,  $Fr_b = 1$  (achieved with  $N_\infty =$   
 161  $1.25 \times 10^{-3} \text{ s}^{-1}$  and  $f = -2 \times 10^{-3} \text{ s}^{-1}$ , leading to a  $S_b = 0.1$ ) in a deep water region  
 162 where  $U_\infty \approx 0.1 \text{ m/s}$  (Mashayek et al., 2024, Figures 1, S1, and S2). We run these sim-  
 163 ulations with six different levels of smoothing, given by values of smoothing scale  $L =$   
 164  $(0, 0.05, 0.1, 0.2, 0.4, 0.8)W$ . Note that, while this set-up does not allow lee waves (since  
 165  $S_b/\delta < 1$ ), we verified that a similar set-up which does support them produces simi-  
 166 lar results (see Section 2 of the Supporting Information).

#### 167 3.1 General dynamics

168 In all simulations in this section, once the initial adjustment period passes, the larger  
 169 scales of the wake are largely time-independent, with the only visible time variability be-  
 170 ing due to small-scale turbulence. While the amount of turbulence is a function of the  
 171 resolved roughness, the seamount-scale dynamics approximately follow the solution by  
 172 Hogg (1973)’s “weak stratification” regime. Namely, the largest feature of the flow is a  
 173 single, isolated, vertically-coherent anticyclone at the top of the seamount — also in ac-  
 174 cordance with Perfect et al. (2018)’s regime expectations. This feature can be seen in  
 175 Figures 1e-f (which shows a vertical average of the vertical vorticity normalized by  $f$ )  
 176 for rough and smooth seamounts, respectively. Even for the rough seamount, this an-  
 177 ticyclone is dominant, with the main difference being its close-following of rough topo-  
 178 graphic contours compared to the smooth version. Differently from the idealized solu-  
 179 tion, but similar to previous simulations Srinivasan et al. (2019, first simulation in their  
 180 Table 1), our simulations exhibit a weak, mostly-cyclonic wake, likely resulting from bot-  
 181 tom drag (Srinivasan et al., 2019).

182 Importantly, the wake has larger values of  $Ro$  for the rough seamount, most ap-  
 183 parent as streaks of anticyclonic vorticity, which are a product of the smaller hori-  
 184 zontal scales present in the rough bathymetry. These higher values of vorticity imprint on  
 185 the Ertel potential vorticity ( $PV = \vec{\nabla}b \cdot [\vec{\nabla} \times \vec{u} + f\vec{k}]$ ), a horizontal-cross section of  
 186 which is shown in Figure 1c-d. Such an imprint leads to streaks in PV that emanate from  
 187 the rough seamount which have been reported in the atmospheric literature, where they

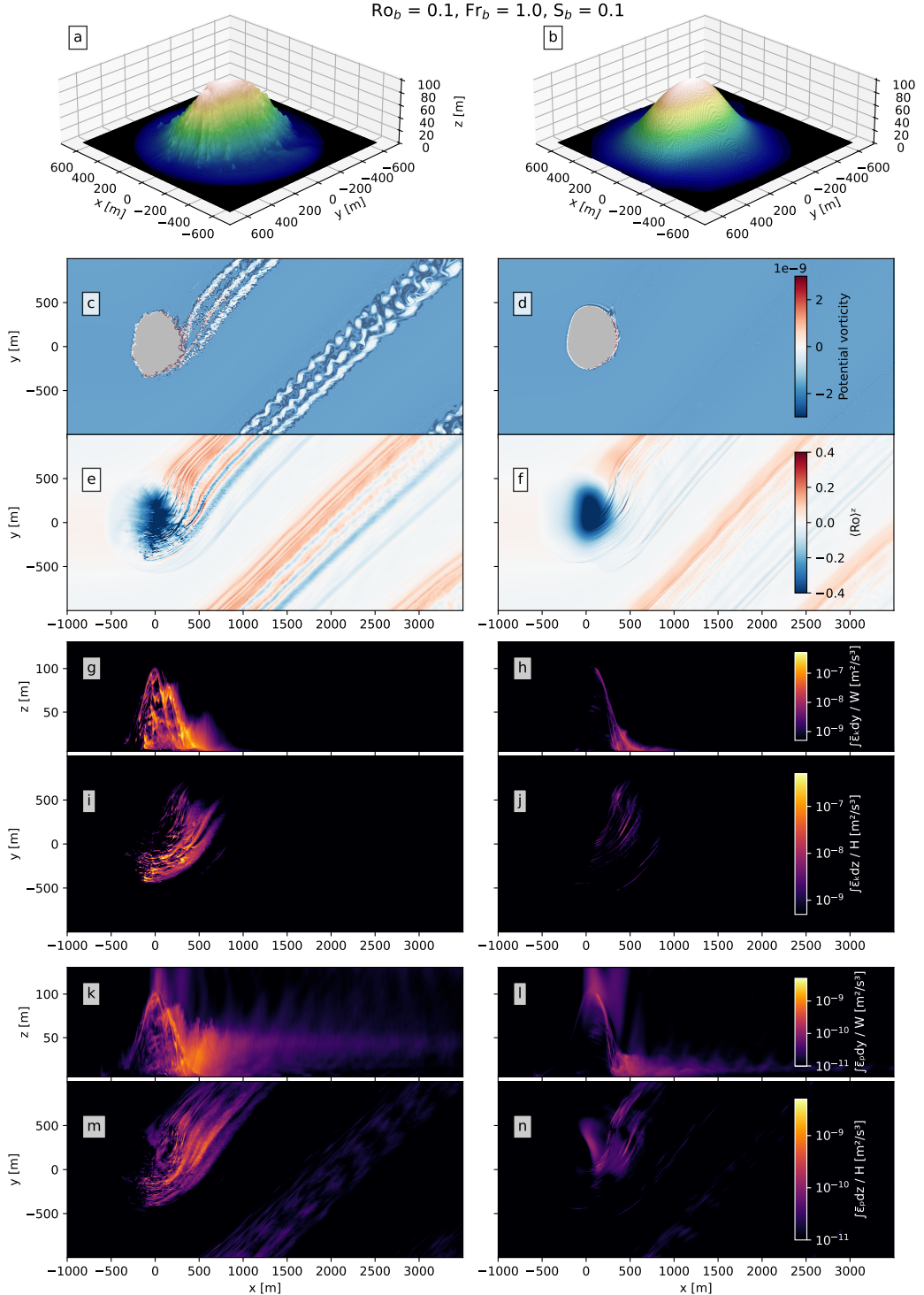


Figure 1: Left column shows results for the a rough seamount ( $L = 0$ ) and right column shows results for a smooth one ( $L = 0.8W$ ). Top row: bathymetry used in the simulations. Second row: instantaneous snapshots of horizontal cross-section of Ertel PV at  $z = H/3$ . Third row: time- and vertically-averaged pointwise Rossby number (vertical vorticity  $/ f$ ). Fourth row: time-averaged, cross-direction-integrated KE dissipation rates. Fifth row: time-averaged, vertically-integrated KE dissipation rates. Sixth row: time-averaged, cross-direction-integrated buoyancy mixing rates. Seventh row: time-averaged, vertically-integrated buoyancy mixing rates.

188 are known as “PV banners” (Schär, 2002; Schär et al., 2003). These banners — absent  
 189 from the smooth bathymetry — have been observed experimentally in atmospheric flows  
 190 (Schär et al., 2003) and are known to affect flow dynamics downstream. Interestingly,  
 191 while PV banners are often observed to have alternating positive-negative PV signals,  
 192 in this case we see alternating positive-zero signals. This is likely due to turbulent mix-  
 193 ing (either due to centrifugal instabilities or 3D turbulence from the seamount bound-  
 194 ary layer) entraining high-PV ambient water, thus bringing negative-PV regions back  
 195 to zero (Haine & Marshall, 1998; Srinivasan et al., 2021; Chor & Wenegrat, 2025).

### 196 3.2 Turbulence and energetics

197 While the large-scale dynamics of the solutions are similar between rough and smooth  
 198 seamounts, the energetics are distinct. Figure 1g-j shows vertical and horizontal profiles  
 199 of KE dissipation rate for both seamounts, and it is clear that the rough bathymetry is  
 200 significantly more dissipative than the smooth one. Furthermore, patches of high dis-  
 201 sipation (in both cases) are co-located with regions of large-magnitude small-scale vor-  
 202 ticity (compare with Figure 1e-f) — a consequence of horizontal shear having a leading  
 203 role in creating turbulence (see Section 3 of the Supporting Information).

204 Moreover, while the peak of KE dissipation  $\varepsilon_k$  happens very close to the seamount  
 205 and is more clearly impacted by the small-scale roughness, large values of buoyancy mix-  
 206 ing  $\varepsilon_p$  tend to be more spread out along the wake. This effect can be seen more clearly  
 207 when comparing Figure 2g,i with Figure 2k,m. Also interesting is the fact that mixing  
 208 happens higher in the water column for the rough case (being concentrated at  $z \approx H/2$ )  
 209 than for the smooth case, where it is mostly concentrated at the bottom, which can be  
 210 seen when comparing panels k and l of the same figure. A similar effect can be seen for  
 211 the KE dissipation, although not as striking. We attribute this effect to the small-scale  
 212 bathymetry prompting a more efficient wake separation, with the flow remaining approx-  
 213 imately attached in the smooth seamount.

214 In order to get a better assessment of the turbulence dependence on smoothness/roughness,  
 215 we plot the normalized, time- and volume-averaged KE dissipation in Figure 2d as a func-  
 216 tion of the normalized smoothing scale  $L/W$  as green circles. It is clear that there is a  
 217 monotonic trend to lower dissipation rates as the bathymetry becomes smoother, with  
 218 a steep initial drop ( $\approx 50\%$ ) already happening for  $L/W = 0.1$ . This difference sta-  
 219 bilizes at around an order of magnitude for  $L/W \approx 0.4$ , and further smoothing does  
 220 not further decrease dissipation. Similar results are shown for mixing as magenta cir-  
 221 cles in the same panel. Although quantitatively not as dramatic as results for dissipa-  
 222 tion, smoothing still accounts for a roughly 3-fold difference in buoyancy mixing. These  
 223 results are independent of seamount orientation, which can be seen in Figure 2d where  
 224 crosses indicate cases run with the bathymetry rotated by  $90^\circ$ . Finally, the top horizon-  
 225 tal axis of Figure 2d shows what the smoothing scale would be for a typical seamount  
 226 of  $W = 10$  km (i.e.  $L^{W=10\text{km}}$ ), revealing that dissipation and mixing are already at a  
 227 minimum with  $L^{W=10\text{km}} = 4$  km. Figure 2d also suggests that resolving bathymetric  
 228 details of approximately  $L^{W=10\text{km}} = 50$  m may be necessary to capture the full effects  
 229 of mixing and dissipation.

## 230 4 Parameter sweep

231 We now examine how roughness influences bulk energetics across various regions  
 232 of the parameter space, characterized here by  $Ro_b$  and  $Fr_b$ . Globally,  $Ro_b$  for seamounts  
 233 typically falls within 0.05–0.5, while  $Fr_b$  is more broadly distributed, generally between  
 234 0.04 and 2 (based on data by Mashayek et al. (2024)). Accordingly, we perform 20 sim-  
 235 ulations covering  $Ro_b = [0.05, 0.1, 0.2, 0.5]$  and  $Fr_b = [0.04, 0.08, 0.3, 1, 2]$ , achieved by  
 236 varying  $f$  and  $N_\infty$ . We estimate the normalized, time-averaged, volume-integrated KE

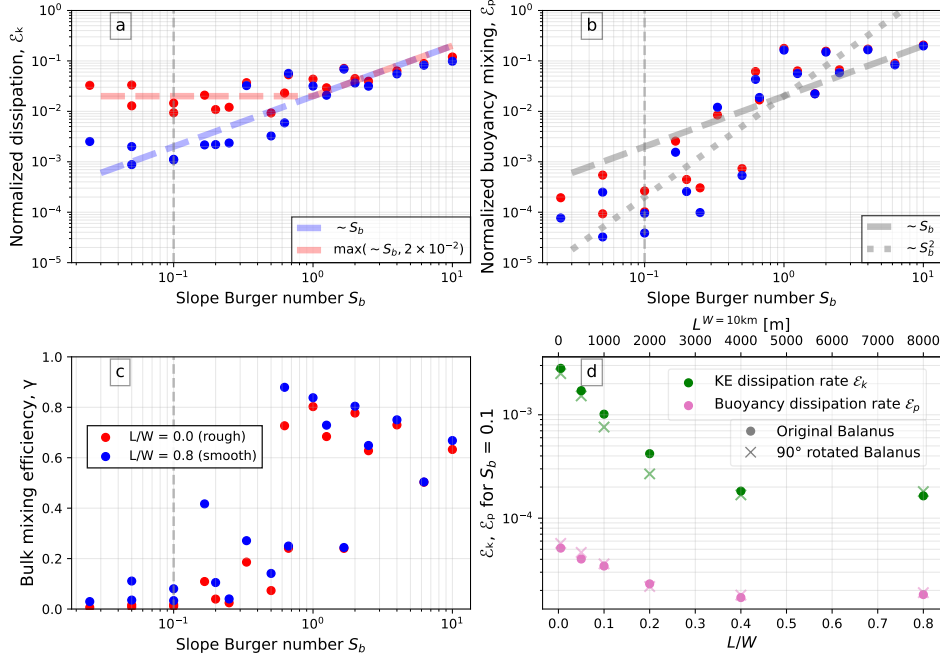


Figure 2: Normalized KE dissipation (panel a), buoyancy mixing (panel b), and mixing efficiency (panel c) as a function of the bathymetric Slope Burger number  $S_b$ . Red points are results from simulations with rough bathymetry (smoothing length scale  $L = 0$ ) and blue points are results from smooth bathymetry (smoothed with a length scale  $L = 0.8W$ ). Dashed and dotted lines are present as references, with their scaling shown in the legend. Panel d shows normalized time- and volume-averaged KE dissipation (green) and buoyancy mixing (magenta) as a function of  $L/W$  for a seamount with  $Rob = 0.1$ ,  $Fr_b = 1$  and  $S_b = 0.1$ . Circles show results for an un-rotated seamount, while crosses show results for 90°-rotated seamount. The top axis in panel d shows the smoothing scale for a typical ocean seamount of  $W = 10$  km,  $L^{10\text{km}}$ . Note that for panel d we consider the un-smoothed bathymetry to have a scale of the grid's horizontal spacing, which equals  $L/W = 0.005$  or  $L^{W=10\text{km}} = 50$  m. Vertical gray dashed lines in panels a, b, and c indicate the parameter regime for results in panel d ( $S_b = 0.1$ ).

dissipation and buoyancy mixing rates resulting from flow-seamount interactions as

$$\mathcal{E}_k = \frac{\iiint \bar{\varepsilon}_k dx dy dz}{U_\infty^3 W^2}, \quad (2)$$

$$\mathcal{E}_p = \frac{\iiint \bar{\varepsilon}_p dx dy dz}{U_\infty^3 W^2}, \quad (3)$$

where  $\bar{(\cdot)}$  is a time-averaging operation, and the normalization comes from assuming  $\iiint (\cdot) dx dy dz \sim L^2 H$  and  $\varepsilon_k \sim U_\infty^3 / H$  — which has been numerically verified. Note that this scaling is slightly different than the one used by Chor and Wenegrat (2025) (who assumed  $\varepsilon_k \sim U_\infty^3 / L$ ), since there is some ambiguity in the definition of the length scale in this case, mostly due to possible changes in the physics with varying  $\delta = H/W$ .

Figure 2a shows results for  $\mathcal{E}_k$  as a function of the bathymetric Slope Burger number  $S_b$ . While it is clear that  $\mathcal{E}_k$  results are organized by  $S_b$ , Figure 2a points to a significant difference between  $\mathcal{E}_k$  generated by rough seamounts in comparison to smooth ones. Namely, for medium to large values of  $S_b$ ,  $\mathcal{E}_k$  scales approximately linearly with Slope Burger number, similar to results observed by Chor and Wenegrat (2025) for a head-

248 land. However, for low values of  $S_b$ , normalized dissipation rates asymptote to a constant  
 249 value of  $\mathcal{O}(10^{-2})$  when using the full resolution topography. Therefore Figure 2a sug-  
 250 gests that the largest relative contribution of small-scale roughness to energetics hap-  
 251 pens for flows with low Slope Burger numbers. Specifically, differences between rough  
 252 and smooth seamount dissipations in Figure 2a for  $S_b \approx 0.1$  are of an order of magni-  
 253 tude, consistent with the results of Section 3.

254 Results for  $\mathcal{E}_p$  are shown in Figure 2b, where an organization with  $S_b$  is also clear  
 255 and, importantly, there is a smaller difference between buoyancy mixing in rough and  
 256 smooth seamounts. Again consistent with Section 3 results, these differences can reach  
 257 a factor of three, and are also more prominent in low- $S_b$  seamounts. Furthermore, in con-  
 258 trast to  $\mathcal{E}_k$ , our results show a dependence of  $\mathcal{E}_p \sim S_b^2$ . This departs from the linear de-  
 259 pendence on  $S_b$  found by Chor and Wenegrat (2025), suggesting a dependence on geom-  
 260 etry for  $\mathcal{E}_p$ . This quadratic scaling for  $\mathcal{E}_p$ , coupled with the linear scaling for  $\mathcal{E}_k$  further  
 261 implies a change in mixing efficiency ( $\gamma = \mathcal{E}_p / (\mathcal{E}_p + \mathcal{E}_k)$ ) with Slope Burger number,  
 262 shown in Figure 2c. Results reveal near-zero  $\gamma$  values for low Slope Burger numbers, with  
 263 mixing efficiency values increasing with increasing  $S_b$ . Mixing efficiency then saturates  
 264 at  $\gamma \approx 1$  for Slope Burger number of unity and higher, which is when the vertical de-  
 265 coupling effect of stratification surpasses the organization effects of rotation. Given that  
 266 high Slope Burger seamounts tend to be concentrated close to the Equator (Mashayek  
 267 et al., 2024, Figure 1E), this implies that low-latitude seamounts may tend to be par-  
 268 ticularly efficient in mixing buoyancy, although that is not pursued further here (see Sec-  
 269 tion 4 of the Supporting Information).

## 270 5 Implications for global energetics

271 Results in Sections 3 and 4 reveal significant differences between rough and smooth  
 272 seamounts. In particular, given the difference in scaling between both cases in Figure  
 273 2a, we are prompted to explore large-scale implications for both configurations. We be-  
 274 gin by approximating the dissipation around both rough and smooth seamounts sepa-  
 275 rately according to

$$\mathcal{E}_k^{\text{smooth}} = 2 \times 10^{-2} S_b, \quad (4)$$

$$\mathcal{E}_k^{\text{rough}} = \max(\mathcal{E}_k^{\text{smooth}}, 2 \times 10^{-2}). \quad (5)$$

276 Both curves are shown in Figure 2a as dashed lines. We can use Equations (2)–(3), along  
 277 with (4)–(5), to estimate the integrated dissipation by each mapped seamount individ-  
 278 ually using data made available by Mashayek et al. (2024), giving us global estimates  
 279 of seamount contributions to dissipation and mixing.

280 Dissipation results are shown in Figure 3a-b for smooth and rough seamounts, re-  
 281 spectively. It is clear that most of the seamount-led dissipation happens in the South-  
 282 ern Ocean regardless of seamount roughness, as expected due to the cubic velocity de-  
 283 pendence in Equation (1). That said, dissipation rates are clearly higher for rough seamounts,  
 284 evident in Figure 3c, which shows zonally-integrated dissipation for both cases. These  
 285 results suggest that seamount roughness (i.e. small-scale bathymetric variability) may  
 286 account for approximately 30% of KE dissipation in the global ocean, and 40% in the  
 287 Southern Ocean specifically.

288 Moreover, these results suggest that small-scale topographic features, while per-  
 289 haps secondary for local dynamics, can change the energetics significantly. Taking the  
 290 dimensions of our geometry and scaling it up to representative Southern Ocean seamount  
 291 sizes ( $\approx 10$  km FWHM; see Figure 2d), our results imply that, by not representing bathy-  
 292 metric details smaller than 500 meters, a model could underestimate dissipation rates  
 293 by 30 to 50% around a given Southern Ocean seamount. This further implies that hor-  
 294 izontal grid spacings of  $\approx 100$  m or smaller are necessary to capture representative seamount  
 295 energetics in the south.

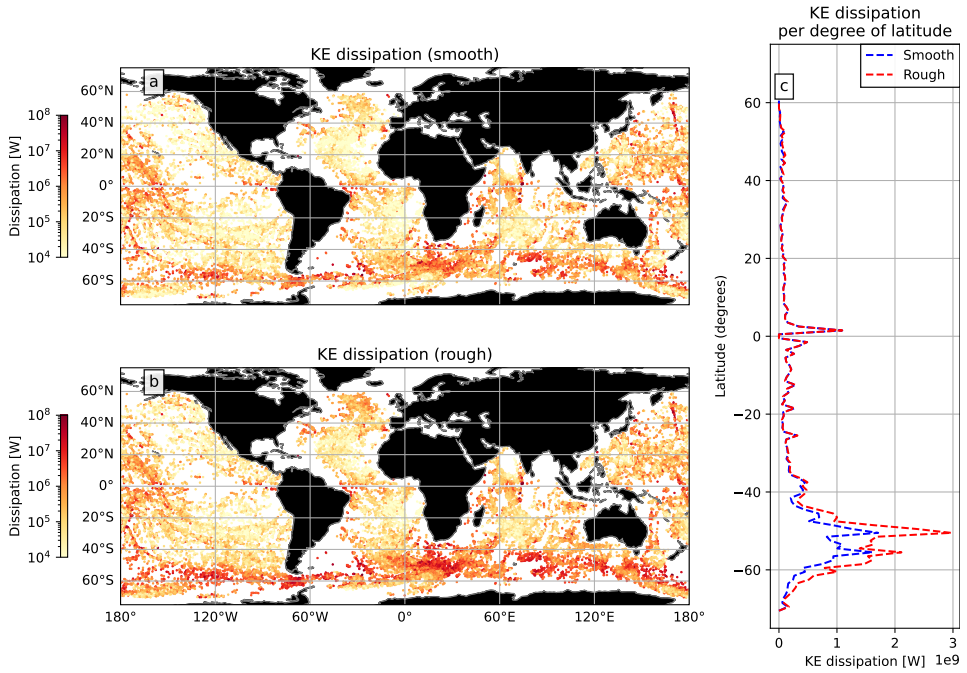


Figure 3: Global integrated seamount dissipation (panels a-b) and mixing (panels d-e). Panel a shows KE dissipation using the scaling for smooth seamounts, while panel b shows the same results using the model for rough seamounts. Panel d shows buoyancy mixing using a linear dependence on  $S_b$ , while panel e shows the same results but assuming a quadratic dependence. Panels c and f show zonally-integrated dissipation and buoyancy per degree of latitude.

Beyond the resolution of the topography itself there may be additional problems with model representation of the forward energy cascade. Although turbulence closures in regional ocean models are generally designed to capture energy production associated with vertical shear, our simulations show that horizontal shear production also plays a significant role (see Section 3 of the Supporting Information). However, horizontal shear production is not accounted for in most commonly-used turbulence closure schemes. As a result, present parameterizations have limited ability to represent the full range of energetics associated with rough seamounts, such that even regional simulations with resolved topography may not appropriately represent wake mixing (cf. Aghor et al. (2025)).

To address this gap, turbulence closures could be expanded in one of two ways: by explicitly including the effects of horizontal shear production, or by parametrizing the impact of unresolved small-scale topography — much like existing wave drag parameterizations (Scinocca & McFarlane, 2000; Jayne & St. Laurent, 2001; Y. Kim et al., 2003; Baker & Mashayek, 2022), some of which incorporate statistical representations of sub-grid scale topography (Lott & Miller, 1997). Implementing these improvements will also require more comprehensive high-resolution bathymetric data to accurately describe sub-grid scale variability, which is presently limited.

## 6 Conclusions

Understanding the energetic impact of seamounts on ocean turbulence and mixing is essential both for our understanding of global dynamics and for accurately representing oceanographic processes in numerical models. Despite the important role played

317 by seamounts as prominent drivers of turbulent dissipation and mixing, the effect of small-  
 318 scale bathymetric roughness on their energetics had not been systematically studied. With  
 319 this in mind, we used turbulence-resolving nonhydrostatic large-eddy simulations to sys-  
 320 tematically explore the difference in energetics between rough and smooth seamounts.

321 Our findings indicate that small-scale bathymetric roughness substantially enhances  
 322 dissipation and mixing in comparison to smooth seamounts. These differences are espe-  
 323 cially evident for seamounts with low Slope Burger numbers ( $S_b \lesssim 1$ ), where kinetic  
 324 energy dissipation can be up to an order of magnitude higher in rough cases, and buoy-  
 325 ancy mixing rates are roughly three times larger. These seamounts are primarily found  
 326 in the Southern Ocean, a region where strong currents make them particularly influen-  
 327 tial in the global energy budget (see Equation (1)). Our results further indicate that omit-  
 328 ting roughness can lead to an underestimation of global ocean dissipation by approxi-  
 329 mately 30%, indicating a leading order effect of small-scale topographic features. Accu-  
 330 rately resolving these effects would require grid resolutions finer than 100 m, which is  
 331 not yet practical for global simulations. Consequently, it is essential that current mod-  
 332 els and their parameterizations properly represent the influence of unresolved roughness  
 333 and turbulence (see discussion in Section 5).

334 While the main simulations in this work do not allow lee waves, their role was in-  
 335 vestigated and found to not significantly alter energetics. With that said, for a sufficiently  
 336 large gap between  $f$  and  $N_\infty$ , roughness may also impact the production of wave energy  
 337 since small-scale waves would be permitted. Given that the smallest possible waves usu-  
 338 ally have length scales of  $\approx 600$  m in the Southern Ocean (Baker & Mashayek, 2022)  
 339 (corresponding to  $L/W \approx 0.05$  for a typical seamount size of  $W = 10$  km), investi-  
 340 gating this topic would have required prohibitively large simulations in our configura-  
 341 tions, and likely requires different methods of investigation. Finally, although not shown  
 342 here, preliminary investigations suggest that the effect of roughness may be more pro-  
 343 nounced (and relevant over larger parts of the parameter space) in shallow water envi-  
 344 ronments — an effect we leave for future studies. We consider both these issues, as well  
 345 as investigations into possible parameterizations for the effects discussed in this manuscript,  
 346 to be important future work with potentially global implications.

## 347 Open Research Section

348 The numerical model simulations upon which this study is based are too large to  
 349 easily archive or transfer. Instead, all the code used to generate the results is available  
 350 at <https://doi.org/10.5281/zenodo.17938969> (Chor, 2025).

## 351 Acknowledgments

352 T. C. and J. O. W. were supported by the National Science Foundation Grant OCE-2242182  
 353 (T. C. and J. O. W.), and Office of Naval Research Grant N000142412583 (J. O. W.).  
 354 GLW's work was supported by Schmidt Sciences, LLC and by the National Science Foun-  
 355 dation grant AGS-183557. We would also like to acknowledge high-performance com-  
 356 puting support from Casper (<https://doi.org/10.5065/qx9a-pg09>) provided by NCAR's  
 357 Computational and Information Systems Laboratory, sponsored by the National Science  
 358 Foundation.

## 359 References

360 Adcroft, A., Hill, C., & Marshall, J. (1997). Representation of topography by shaved  
 361 cells in a height coordinate ocean model. *Monthly Weather Review*, 125(9),  
 362 2293 - 2315. doi: 10.1175/1520-0493(1997)125<2293:ROTBSC>2.0.CO;2  
 363 Aebischer, U., & Schär, C. (1998). Low-level potential vorticity and cyclogenesis to  
 364 the lee of the alps. *Journal of the Atmospheric Sciences*, 55(2), 186–207. doi:

365 10.1175/1520-0469(1998)055<0186:LLPVAC>2.0.CO;2  
 366 Aghor, P. P., McKinley, M., & Bracco, A. (2025). Interaction of ocean currents and  
 367 seamounts: Role of bottom topography around atlantis ii. *ESS Open Archive*.  
 368 doi: 10.22541/essoar.175285275.52840024/v1

369 Baker, L. E., & Mashayek, A. (2022). The impact of representations of realistic to-  
 370 pography on parameterized oceanic lee wave energy flux. *Journal of Geophysical*  
 371 *Research: Oceans*, 127(10), e2022JC018995. doi: 10.1029/2022JC018995

372 Bou-Zeid, E., Meneveau, C., & Parlange, M. (2005, 01). A scale-dependent la-  
 373 grangian dynamic model for large eddy simulation of complex turbulent flows.  
 374 *Physics of Fluids*, 17(2), 025105. doi: 10.1063/1.1839152

375 Chamecki, M., Chor, T., Yang, D., & Meneveau, C. (2019). Material transport in  
 376 the ocean mixed layer: recent developments enabled by large eddy simulations.  
 377 *Reviews of Geophysics*, 57(4), 1338–1371.

378 Chor, T. (2025). *Code for the paper “Turbulent mixing and dissipation around rough*  
 379 *seamounts”*. Zenodo. Retrieved from 10.5281/zenodo.17938969 doi: 10  
 380 .5281/zenodo.17938969

381 Chor, T., & Wenegrat, J. O. (2025). The turbulent dynamics of anticyclonic sub-  
 382 mesoscale headland wakes. *Journal of Physical Oceanography*, 55(6), 737 - 759.  
 383 doi: 10.1175/JPO-D-24-0139.1

384 Gula, J., Molemaker, M. J., & McWilliams, J. C. (2016). Topographic generation of  
 385 submesoscale centrifugal instability and energy dissipation. *Nature communica-  
 386 tions*, 7(1), 1–7. doi: 10.1038/ncomms12811

387 Haine, T. W., & Marshall, J. (1998). Gravitational, symmetric, and baroclinic insta-  
 388 bility of the ocean mixed layer. *Journal of physical oceanography*, 28(4), 634–  
 389 658.

390 Hogg, N. G. (1973). On the stratified taylor column. *Journal of Fluid Mechanics*,  
 391 58(3), 517–537. doi: 10.1017/S0022112073002302

392 Jalali, M., & Sarkar, S. (2017). Large eddy simulation of flow and turbulence at the  
 393 steep topography of luzon strait. *Geophysical Research Letters*, 44(18), 9440–  
 394 9448. doi: 10.1002/2017GL074119

395 Jayne, S. R., & St. Laurent, L. C. (2001). Parameterizing tidal dissipation over  
 396 rough topography. *Geophysical Research Letters*, 28(5), 811–814. doi: <https://doi.org/10.1029/2000GL012044>

397 Kim, S., & Wessel, P. (2011). New global seamount census from altimetry-derived  
 398 gravity data. *Geophysical Journal International*, 186(2), 615–631. doi: 10  
 399 .1111/j.1365-246X.2011.05076.x

400 Kim, Y., Eckermann, S. D., & Chun, H. (2003). An overview of the past,  
 401 present and future of gravity-wave drag parametrization for numerical cli-  
 402 mate and weather prediction models. *Atmosphere-Ocean*, 41(1), 65–98. doi:  
 403 10.3137/ao.410105

404 Kleissl, J., Kumar, V., Meneveau, C., & Parlange, M. B. (2006). Numerical study  
 405 of dynamic smagorinsky models in large-eddy simulation of the atmospheric  
 406 boundary layer: Validation in stable and unstable conditions. *Water resources*  
 407 *research*, 42(6). doi: 10.1029/2005WR004685

408 Liu, J., Putman, P., & Sarkar, S. (2024). Effect of rotation on wake vortices in strati-  
 409 fied flow. *Journal of Fluid Mechanics*, 999, A44. doi: 10.1017/jfm.2024.721

410 Lott, F., & Miller, M. J. (1997). A new subgrid-scale orographic drag parametriza-  
 411 tion: Its formulation and testing. *Quarterly Journal of the Royal Meteorologi-  
 412 cal Society*, 123(537), 101–127. doi: 10.1002/qj.49712353704

413 Mashayek, A., Gula, J., Baker, L. E., Naveira Garabato, A. C., Cimoli, L., Riley,  
 414 J. J., & de Lavergne, C. (2024). On the role of seamounts in upwelling deep-  
 415 ocean waters through turbulent mixing. *Proceedings of the National Academy*  
 416 *of Sciences*, 121(27), e2322163121. doi: 10.1073/pnas.2322163121

417 Mellor, G. L., Oey, L.-Y., & Ezer, T. (1998). Sigma coordinate pressure gradient  
 418 errors and the seamount problem. *Journal of Atmospheric and Oceanic Tech-*  
 419

nology, 15(5), 1122 - 1131. doi: 10.1175/1520-0426(1998)015<1122:SCPGEA>2.0.CO;2

Munk, W., & Wunsch, C. (1998). Abyssal recipes ii: energetics of tidal and wind mixing. *Deep Sea Research Part I: Oceanographic Research Papers*, 45(12), 1977-2010. doi: doi.org/10.1016/S0967-0637(98)00070-3

Nagai, T., Hasegawa, D., Tsutsumi, E., Nakamura, H., Nishina, A., Senju, T., ... Tandon, A. (2021). The kuroshio flowing over seamounts and associated submesoscale flows drive 100-km-wide 100-1000-fold enhancement of turbulence. *Communications Earth & Environment*, 2(1), 1-11.

Nikurashin, M., Ferrari, R., Grisouard, N., & Polzin, K. (2014). The impact of finite-amplitude bottom topography on internal wave generation in the southern ocean. *Journal of Physical Oceanography*, 44(11), 2938 - 2950. doi: 10.1175/JPO-D-13-0201.1

Perfect, B., Kumar, N., & Riley, J. (2018). Vortex structures in the wake of an idealized seamount in rotating, stratified flow. *Geophysical Research Letters*, 45(17), 9098-9105. doi: 10.1029/2018GL078703

Perfect, B., Kumar, N., & Riley, J. (2020a). Energetics of seamount wakes. Part I: Energy exchange. *Journal of Physical Oceanography*, 50(5), 1365-1382. doi: 10.1175/JPO-D-19-0105.1

Perfect, B., Kumar, N., & Riley, J. (2020b). Energetics of seamount wakes. Part II: Wave fluxes. *Journal of Physical Oceanography*, 50(5), 1383-1398. doi: 10.1175/JPO-D-19-0104.1

Puthan, P., Pawlak, G., & Sarkar, S. (2022). Wake vortices and dissipation in a tidally modulated flow past a three-dimensional topography. *Journal of Geophysical Research: Oceans*, 127(8), e2022JC018470. doi: 10.1029/2022JC018470

Ramadhan, A., Wagner, G. L., Hill, C., Campin, J.-M., Churavy, V., Besard, T., ... Marshall, J. (2020). Oceananigans.jl: Fast and friendly geophysical fluid dynamics on GPUs. *Journal of Open Source Software*, 5(53), 2018.

Ryan, W. B. F., Carbotte, S. M., Coplan, J. O., O'Hara, S., Melkonian, A., Arko, R., ... Zemsky, R. (2009). Global multi-resolution topography synthesis. *Geochemistry, Geophysics, Geosystems*, 10(3). doi: 10.1029/2008GC002332

Schär, C. (2002). Mesoscale mountains and the larger-scale atmospheric dynamics: A review. In R. Pearce (Ed.), *Meteorology at the millennium* (Vol. 83, p. 29-42). Academic Press. doi: 10.1016/S0074-6142(02)80155-3

Schär, C., Sprenger, M., Lüthi, D., Jiang, Q., Smith, R. B., & Benoit, R. (2003). Structure and dynamics of an alpine potential-vorticity banner. *Quarterly Journal of the Royal Meteorological Society*, 129(588), 825-855. doi: 10.1256/qj.02.47

Scinocca, J. F., & McFarlane, N. A. (2000). The parametrization of drag induced by stratified flow over anisotropic orography. *Quarterly Journal of the Royal Meteorological Society*, 126(568), 2353-2393. doi: 10.1002/qj.49712656802

Sikirić, M. D., Janeković, I., & Kuzmić, M. (2009). A new approach to bathymetry smoothing in sigma-coordinate ocean models. *Ocean Modelling*, 29(2), 128-136. doi: 10.1016/j.ocemod.2009.03.009

Srinivasan, K., McWilliams, J. C., & Jagannathan, A. (2021). High vertical shear and dissipation in equatorial topographic wakes. *Journal of Physical Oceanography*, 51(6), 1985-2001. doi: 10.1175/JPO-D-20-0119.1

Srinivasan, K., McWilliams, J. C., Molemaker, M. J., & Barkan, R. (2019). Submesoscale vortical wakes in the lee of topography. *Journal of Physical Oceanography*, 49(7), 1949-1971. doi: 10.1175/JPO-D-18-0042.1

Wagner, G. L., Silvestri, S., Constantinou, N. C., Ramadhan, A., Campin, J.-M., Hill, C., ... Ferrari, R. (2025). High-level, high-resolution ocean modeling at all scales with Oceananigans. *arXiv preprint*. doi: 10.48550/arXiv.2502.14148

Waterhouse, A. F., MacKinnon, J. A., Nash, J. D., Alford, M. H., Kunze, E., Sim-

475 mons, H. L., ... Lee, C. M. (2014). Global patterns of diapycnal mixing from  
476 measurements of the turbulent dissipation rate. *Journal of Physical Oceanogra-*  
477 *phy*, 44(7), 1854 - 1872. doi: 10.1175/JPO-D-13-0104.1

478 Wright, C. J., Scott, R. B., Ailliot, P., & Furnival, D. (2014). Lee wave generation  
479 rates in the deep ocean. *Geophysical Research Letters*, 41(7), 2434-2440. doi:  
480 10.1002/2013GL059087